Journal of the European Ceramic Society 44 (2024) 4853–4862

Contents lists available at ScienceDirect

Journal of the European Ceramic Society

journal homepage: www.elsevier.com/locate/jeurceramsoc

Determination of short carbon fiber orientation in zirconium diboride ceramic matrix composites

Laura Silvestroni [a,1], Andreas Kupsch [b,*,2], Bernd R. Müller [b,3], Alexander Ulbricht [b,4], Frank Wieder [b,5], Tobias Fritsch [b,6], Diletta Sciti [a,7], Giovanni Bruno [b,c,8]

[a] CNR-ISSMC (former ISTEC), Institute of Science, Technology and Sustainability for Ceramics, Via Granarolo 64, Faenza 48018, Italy
[b] BAM, Bundesanstalt für Materialforschung und -prüfung, Unter den Eichen 87, Berlin 12205, Germany
[c] University of Potsdam, Institute of Physics and Astronomy, Karl-Liebknecht-Str.25-26, Potsdam 144756, Germany

ARTICLE INFO

Keywords:
Ceramic matrix composites
Synchrotron X-ray refraction radiography
X-ray computed tomography
Scanning electron microscopy
High-temperature ceramics

ABSTRACT

In fiber-reinforced components, the fiber alignment and orientation have paramount influence on the thermo-mechanical properties of the resulting composite, for both short and continuous fiber. Here we present the case of an ultra-refractory matrix intended for extreme environment applications, ZrB_2, reinforced with 20 vol% and 50 vol% short carbon fibers. In both cases, fibers tend to align perpendicular to the uniaxial pressure applied during shaping and sintering of a pellet, although the fiber tilt across the pellet thickness is difficult to determine. Moreover, for high volume fractions of reinforcement, the spatial distribution of the fibers is heterogeneous and tends to have domains of preferential orientations. We compare the information on the fiber distribution as collected by scanning electron microscopy images, X-ray computed tomography and synchrotron X-ray refraction radiography (SXRR). The three techniques prove to be complementary.

Importantly, we demonstrate that SXRR yields the most statistically significant information due to the largest field of view, yet with a sensitivity down to the nanometer, and that can be successfully applied also to heavy matrix materials, such as zirconium boride.

1. Introduction

Ultra-high temperature ceramics (UHTCs), and particularly zirconium diboride, ZrB_2, are regarded as the most promising materials for use in harsh environments, owing to their high melting point (over 3000°C), high refractoriness (up to 2100°C), ablation resistance, and metal-like thermal conductivity [1–5]. To overcome the intrinsic brittleness of UHTCs, recent investigations have proven that the introduction of fibers, either continuous or discontinuous, tremendously improve the failure tolerance over a broad temperature range without hampering the hot corrosion resistance [6–8]. It has been also highlighted that the fiber distribution and architecture impact the final mechanical and thermo-mechanical properties of the ceramic matrix composite (CMC) [9–14], no matter if the matrix is a polymer, a metal or a ceramic [15,16].

The fiber orientation in continuous fiber reinforced CMCs is well clear and only minimal discrepancies from the target fiber orientation (0°, 90°, Bouligand) are found upon following a suitable processing layup method. The great versatility of short fiber reinforced composites [9,10,17,18] relates indeed to the easiness of the process. Such process follows typical powder metallurgical routes that comprise conventional ball milling , wet or dry shaping technologies, including slip casting and

* Corresponding author.
E-mail address: andreas.kupsch@bam.de (A. Kupsch).
[1] ORCID LS 0000-0003-4595-0299
[2] ORCID AK 0000-0002-1585-1743
[3] ORCID BRM 0000-0003-2234-1538
[4] ORCID AU 0000-0003-3505-1716
[5] ORCID FW 0000-0001-6718-7314
[6] ORCID TF 0000-0002-0472-2874
[7] ORCID DS 0000-0002-3836-6118
[8] ORCID GB 0000-0001-9632-3960

https://doi.org/10.1016/j.jeurceramsoc.2024.02.048
Received 21 November 2023; Received in revised form 15 February 2024; Accepted 21 February 2024
Available online 23 February 2024

3D printing, and sintering by hot pressing or spark plasma sintering. Such processes allow remarkable cost reduction of the manufacturing line as compared to continuous fiber CMCs. It is to remark, though, that in the preparation of simple shaped pellets through pressing of dry powder-fiber mixtures, the distribution and orientation of the fiber is not predictable, since parameters such as fiber volume fraction and fiber length come into play.

Experimental research has shown that, due to processing including milling and linear pressing, the fiber length reduces from the nominal 3 mm to 150–300 μm length [19–21]. Then, for such short fibers, agglomeration is generally not observed for fiber volume fraction between 5 and 60 vol%, but the fibers tend to align their long axis perpendicular to the direction of applied pressure. For the sake of clarity and to avoid misunderstanding with the instrumental axis systems, the labeling "surface" will be henceforth used to refer to the plane perpendicular to the pressure axis, and "cross" will refer to planes parallel to the pressure axis, like sketched in Fig. 1.

Conversely, in the cross plane section, parallel to the pressure axis (see Fig. 1), the orientation distribution of the fibers seems almost isotropic. For low fiber contents, 5–20 vol%, the fibers are distant from one another and tilting may occur along the pellet thickness. On the other hand, for high volume fractions, i.e., above 30 vol%, the fibers tend to build networks, forming domains of iso-oriented fibers.

Having a clear picture of the fiber orientation within the sintered pellet is of importance first for the resulting thermo-mechanical properties, and then, from a design and modeling perspective, for the determination of the critical fiber fraction threshold allowing tailored preferential distributions. Indeed, knowledge of the orientation distribution of fibers can be fed into numerical simulations that support and rationalize time-consuming and expensive experimental campaigns in materials engineering [22].

The precise determination of the fiber orientation distribution in CMCs is still a challenge, especially in heavy matrix materials such as ZrB_2. Several techniques can be adopted to tackle the problem. The most common ones are image analysis of micrographs taken by optical or scanning electron microscopy (SEM) images, [23] and X-ray computed tomography (XCT) [24–32]. Recently, synchrotron X-ray refraction radiography (SXRR, see [33,34]) has been successfully utilized for similar tasks, e.g., the damage of glass fibers in dental posts after trimming, [35] or the pore orientation in porous ceramics [36]. All methodologies have their advantages and drawbacks, as summarized in Table 1, therefore, a careful choice must be made according to the material and the problem to be solved. When possible, a combination of such techniques should be preferred.

Image analysis of micrographs is a viable route, it gives accurate 2D outputs and is adaptable to any kind of matrix, plastic, metal, ceramic, that might present other relevant microstructural features such as second phase, pores or flaws. However, to gain sufficient statistics, time consuming procedures of surface polishing, adequate imaging, and software analysis are needed (e.g., image stitching, artifact correction). One must also keep in mind that no standard for this method is currently available.

XCT provides 3D information over macroscopic volumes, i.e., > 1 mm linear size. Its resolution depends on the specimen size, and for specimens of a few mm diameter, a resolution of a few microns can be achieved. Tomograms are obtained from the reconstruction of some thousands X-ray radiographs recorded under different projection angles.

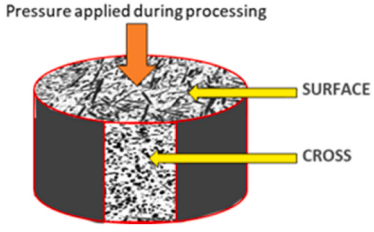

Fig. 1. Sketch of the fiber arrangement in the sintered pellet reinforced with short fiber and corresponding nomenclature used in this work.

Table 1
Advantages and disadvantages of various methods for determining fiber orientation in CMCs.

Method	Advantages	Disadvantages
Optical microscopy / SEM	• accurate • all kinds of matrix materials	• small field of view • time consuming • metallographic sample preparation • standardization needed • 2D
XCT	• 3D visualization	• Small field of view at high resolution
SXRR	• 2.5D • sensitive to interfaces and their orientation • large field of view • reliable statistics	• restricted to platelet-shaped specimens

SXRR is an advanced 2D X-ray imaging technique, which exploits the refraction of X-rays at interfaces between materials with different electron density. The deflection of X-rays can be calculated by means of Snell's law [37], analogous to the refraction of visible light with the major difference that the real part of the refraction index, n, in the X-ray region is smaller than 1, i.e., $n = 1 - \delta$, where δ is the so-called refraction decrement. Since δ is very small, in the order of 10^{-7} - 10^{-6}, the deflection angles are also very small, some arc minutes. This fact has hindered a wide use of the technique. However, SXRR enables the detection of defects, such as pores or cracks, smaller than the spatial resolution of the imaging system, typically 1–5 μm, and has been recently perfectioned to this end [34,38]. Moreover, SXRR can also be combined with load and temperature stages to perform in-situ experiments to reveal the onset of cracks in fiber-reinforced plastics [39], the damage evolution in metal matrix composites under tensile load [40], or the evolution of different types of porosity in additively manufactured alloys during heat treatment [41]. Recently, a synchrotron X-ray refraction tomography study was also crucial in quantifying the hydrogen-assisted microcracking in duplex stainless steel by 3D SXRR imaging [42].

The purpose of this paper is to compare and discuss the three methodologies outlined above to determine the orientation of short fibers, 150–300 μm long, dispersed in low and high-volume fractions within a black ceramic matrix, ZrB_2. We show that one technique alone cannot provide the complete picture, and often the combination of two, or even more, is necessary to avoid misinterpretations.

2. Experimental

Ceramic materials were prepared starting from commercial powders and fibers. As a matrix, ZrB_2 (Grade B, H.C. Starck GmbH, Goslar, Germany) and 5 vol% Si_3N_4 (Bayer AG, Leverkusen, Germany) was chosen, while, as reinforcement, commercial chopped pitch-derived carbon fibers (Granoc HN-80-C, Nippon Graphite Fiber Co., Ltd., Himeji, Japan, diameter: 7–10 μm and nominal chopped length 3 mm) in 20 vol% and 50 vol% of the whole ceramic powders were added. The powder mixtures were ball milled for 24 h in pure ethanol using silicon carbide as milling media. After 2 hours milling, the target amount of fiber was added stepwise to the slurries and let mill for another 22 hours. Subsequently, the slurries were dried in a rotary evaporator and hot pressed in low vacuum using an induction-heated graphite die with a uniaxial pressure of 30 MPa at 1900°C. The two CMC materials were labeled ZB20 and ZB50 for 20 vol% and 50 vol% of fibers fraction, respectively.

2.1. Scanning electron microscopy (SEM)

The microstructure was analyzed on polished surfaces by field emission scanning electron microscopy (FE-SEM, Carl Zeiss Sigma NTS GmbH, Oberkochen, Germany) equipped with energy dispersive X-ray spectroscopy (EDS, INCA Energy 300, Oxford Instruments plc, UK).

Key microstructural features, such as actual fiber volume fraction, fiber apparent length (i.e., Feret's maximum length), misorientation angle with respect to the axis perpendicular to the hot press direction, and Feret aspect ratio were evaluated using commercial software (Image Pro Plus, v.7, Media Cybernetics, MD, USA, and Avizo 3D, 2021.2, Thermo Fisher Scientific, France). For the purpose, SEM images with 1000× magnification were acquired on the cross planes, then each image was binarized using threshold filters and considering objects with diameter above 4 μm. At least 1200 objects were considered for each material.

2.2. X-ray computed tomography (XCT)

For XCT, match-like specimens were extracted from the sintered pellets by conventional diamond rotary blade. The matchstick specimens had a final size of 17.4 mm × 2.5 mm × 2.0 mm.

To visualize the fiber distribution within the material, X-ray computed tomography scans were conducted using a laboratory XCT scanner (GE V|tome|x L 180/300, GE Sensing and Inspection GmbH, Wunstorf, Germany), Fig. 2a. The scanner's transmission X-ray tube was used at 110 kV and 100 μA (voltage and cathodic current). A source-to-object distance (SOD) of 4 mm and a source-to-detector distance (SDD) of 480 mm were used, resulting in a magnification factor of 120. The detector (with a pixel pitch of 400 μm) was binned in 2×2 elements, leading to a reconstructed voxel size of 3.3 μm linear size. The spatial resolution in a single projection was determined by using a JIMA RC-02 resolution chart [43]. 1500 images were acquired over a 360° rotation at an exposure time of 2 s. The reconstruction of the data set was performed using the Feldkamp algorithm [44] implemented in the software package VGSTUDIOMAX 2023.1 (Volume Graphics GmbH, Heidelberg, Germany). The analysis of the fiber orientation was performed using the fiber orientation module of the same software package.

2.3. Synchrotron X-ray refraction radiography (SXRR)

For the SXRR measurements, the XCT specimens were thinned with grinding abrasive paper to 17.4 mm × 2.5 mm × 0.56 mm (ZB20) and 0.52 mm (ZB50).

For the analysis of the local distribution of sub-micrometer objects not visible by XCT, SXRR was carried out at the beam line BAM*line* of the electron storage ring BESSY II (Helmholtz-Zentrum, Berlin, Germany) [45,46]. The Diffraction Enhanced Imaging (DEI) setup was used [47–49]. The basic setup is presented in Fig. 2b, and the principle of this technique is described in [38]. A Si(111) single crystal analyzer is placed between the specimen and the detector to filter the X-rays according to their propagation direction. By scanning the rocking curve (RC) of the analyzer crystal over a small angular tilt range, typically about 1 arc minute, one collects the refraction signal generated by internal surfaces (e.g., cracks, pores, fibers). Refraction events within the specimen cause X-rays to be deflected from their original path and, thus, the X-ray divergence is increased with respect to the free X-ray beam, used as a reference and also called the flat field signal. The analyzer crystal selects the X-rays within its scattering plane (y-z-plane in Fig. 2b, spanned by the incident beam and the scattering vector **Q**, see Fig. 2b, of the analyzer crystal, i.e., the (111) reciprocal lattice vector). Consequently, only interfaces oriented within the x-z-plane in Fig. 2b can be detected, with a tolerance of about ±45°. Because of this property, the SXRR technique is well suited to determine the local orientation of internal interfaces, such as cracks or fiber/matrix interfaces, and to derive a measure of the global fiber orientation in the specimen by integration over the whole image.

For the measurements performed in this study, a photon energy of 50 keV was selected using a Si(111) double-crystal monochromator. The sample transmission was about 10%. The details of the setup are given in [34,50]. The effective pixel size was about 4 μm. The primary beam was narrowed to the specimen size (6 mm vertical, 2.5 mm horizontal) to suppress detector backlighting [51,52]. The two specimens were mounted close to each other in a slide frame and measured simultaneously, see Fig. 2b. In a first measurement, the analyzer crystal was tilted in 41 steps with a step size of $\Delta\theta = 0.0001°$ around the X-axis (perpendicular to the X-ray beam) in the vicinity of the Bragg angle ($\theta_B = 2.2664°$ at 50 keV). After each step, a refraction image of the specimens was recorded. For each pixel of the detector, a spatially correlated rocking curve was created. The corrected rocking curve images were analyzed with an in-house developed software code based on Python [53]. The maximum intensity (I_{max}) and the integral intensity (I_{int}) of the rocking curve for each pixel of the camera were determined. The local refraction value, $C{\cdot}d$, and the local absorption property, $\mu{\cdot}d$, of the specimens of thickness d, were calculated with the following formulae:

$$C \bullet d = 1 - \frac{I_{max} \bullet I_{int,0}}{I_{max,0} \bullet I_{int}} \quad (1)$$

$$\mu \bullet d = \ln\left(\frac{I_{int,0}}{I_{int}}\right) \quad (2)$$

where the index 0 refers to the reference measurement performed without the specimen in the beam. C is proportional to the internal specific surface, i.e., the surface per unit volume in the beam path. To eliminate the influence of the specimen thickness on C, it is common practice to divide Eq. (1) by Eq. (2). C/μ gives the normalized refraction value, hereafter referred to as "relative specific surface" (please note that C/μ is non-dimensional and, therefore, only proportional to the specific surface, which has dimensions of m^{-1}).

In a second set of measurements, to determine the fiber orientation in

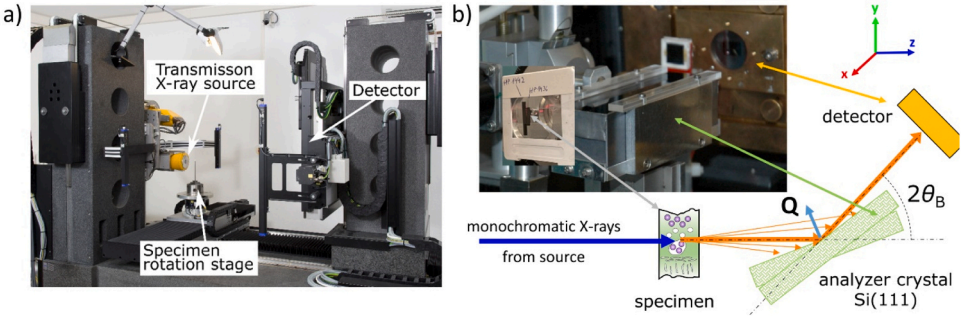

Fig. 2. a) Experimental set up for XCT measurements (GE V|tome|x L 180/300). b) Schematic representation of the SXRR experimental setup and a photograph of the instrumentation at the beam line BAM*line*. The specimens are mounted on a slide frame.

the cross plane, the specimens were rotated over 360° around the z axis, Fig. 2, with angular increments of 1°. Since recording full RCs would have been too time consuming, images were only acquired in the RC center (obtaining I_{max} and $I_{max,0}$). In such conditions, all X-rays deflected by refraction events within the specimen are rejected by the analyzer crystal, causing a seemingly additional attenuation of the X-rays. Lacking the RC integrals, the ratio ($I_{max,0}/I_{max}$), the apparent transmission, was used to characterize the fiber orientation [54–57].

3. Results and discussion

An overview of the materials properties collected in previous studies [21,22], including density, as measured by Archimedes' method, and the main thermo-mechanical properties measured in different orientations, is provided in Table 2. The thermal expansion and the thermal conductivity are indeed different in directions parallel or perpendicular to the pressure axis.

3.1. Fiber misorientation: analysis of SEM images

Examples of the microstructure of the ZB20 and ZB50 CMCs in the cross plane are displayed in Fig. 3. SEM images show crack-free materials, without fiber agglomeration, but with preferential orientation along the surface plane: most of the fibers align perpendicular to the pressure axis during shaping and sintering. On the contrary, no preferential orientation in the cross plane could be visually appreciated .

Image analysis carried out on SEM micrographs of the cross planes was time consuming and very much stochastic within the portion of material analyzed, which comprised about 1200 fibers.

Fig. 4a shows examples of SEM images. Their analysis was carried out according to the method explained in Section 2.1 and the results plotted in Fig. 4b, c. For the ZB20 specimen, the total area of the ellipses corresponds to about 20% of the image area, in agreement with the nominal volume fraction of the fibers (20 vol%). For the ZB50 specimen, the measured total fiber fraction was around 46 vol%, slightly lower than the nominal 50%. This discrepancy has two possible explanations: during processing fiber milling could have caused production of submicrometric debris, such debris is excluded in the computation; sintering at high temperatures might have caused some fiber edge corrosion, as reported in [58]; both phenomena would cause an underestimation of the actual volume fraction.

The Feret aspect ratio is defined as the ratio of the long to the short axis of an approximated ellipse, i.e., an aspect ratio of 1 corresponds to a circle. It is observed that both specimens have similar fiber shape distribution, and that most of intersected fibers show a Feret aspect ratio between 1 and 2.5.

About 75% of the ellipses had an angle of 90° ± 20° to the pressure axis in ZB20, 82% in ZB50. This indicates that the identified fibers were predominantly oriented parallel to the surface plane of the pellet, see Fig. 1 for reference. Interestingly enough, there seems to be a relation between the apparent fiber length (largest Feret's length) and the orientation angle. This is plotted in Fig. 4c: the longer the fiber (or ellipsoid), the smaller its ability to deviate from a parallel orientation to the surface during processing (angle to the pressure direction = 90°).

Overall, the analysis of SEM images enables quantifying small differences in the fiber orientation between ZB20 and ZB50. This could, however, be obtained only upon labor intensive (manual) image segmentation and statistical analysis.

3.2. Fiber misorientation: XCT

Fig. 5 and Fig. 6 show exemplary images based on XCT reconstructions: a surface plane and two cross planes, as reconstructed from the XCT dataset of the two materials.

To exclude edge effects in the determination of the fiber orientation, the quantitative analysis was performed on an inner fraction of the specimens' volume.

The results for ZB20 and ZB50 are shown in Fig. 7 and Fig. 8, respectively. The fibers are color-coded according to their orientation angle with respect to the pressure axis. Most of the fibers are colored in red, which corresponds to fibers oriented nearly perpendicular to the pressure axis.

The fiber volume content was calculated as 20.95 vol% for ZB20, compared to a nominal 20 vol%, and as 49.17 vol% for ZB50, compared to a nominal 50 vol%. The experimental values perfectly agree well with the nominal ones.

Additionally, the analysis provides histograms of the local fiber orientation, as depicted in Fig. 9. The alignment of fibers perpendicular to the pressure axis is more pronounced in specimen ZB20, where the initially loose packing enables misoriented fibers to be aligned under load. This is quantified by the percentiles given in Table 3. The corresponding full widths at half maximum obtained from fitting Pseudo Voigt functions [53] to the angular distribution of fibers are 43.6° for ZB20 and 49.7° for ZB50.

Moreover, a mean orientation tensor (MOT) M is generated (see Table 3 for the results). Tensor components M_{ij} with $i \neq j$ are close to zero and can be neglected. The relation $M_{11} \sim M_{22} > M_{33}$ indicates a nearly ideal cylindrical symmetry of the fiber orientation (with the pressure axis being the symmetry axis) .

3.3. Fiber misorientation: SXRR

After the XCT measurement, platelets were cut from the specimens in such a way that the SXRR analysis of these tiles (Fig. 10) could be compared to virtual cross sections of the XCT reconstructions (see Fig. 5b and Fig. 6b). Since the SXRR technique is sensitive to the orientation of the interfaces, full RCs of both specimens were first measured in two orthogonal orientations, i.e., with the fibers parallel and perpendicular to the scattering vector. Fig. 10 shows the color-coded 2D distribution of the relative specific surface, C/μ, for the two orientations.

In both orientations, the C/μ values are not homogeneously distributed over the gauge volume. The respective C/μ values averaged over the whole images of Fig. 10a are shown in Fig. 10b. The inhomogeneities of the C/μ values over the measurement volumes are shown as error bars.

Both specimens show the largest C/μ mean value for the fibers oriented perpendicular to the scattering vector **Q**. Due to the higher fiber

Table 2
Experimental density (ρ) and typical mechanical properties of ZrB_2 ceramics containing 20 vol% and 50 vol% chopped carbon fiber [21]. σ: 4-pt bending strength, K_{Ic}: fracture toughness measured at room temperature (RT) and at 1500°C under Ar atmosphere, E: Young's modulus at room temperature, α: coefficient of thermal expansion averaged between RT and 1300°C, measured parallel (‖) or perpendicular (⊥) to the pressure axis, K_{TH}: thermal conductivity averaged between RT and 1950°C.

Label	ρ g/cm^3	σ_{RT} MPa	σ_{1500} MPa	$K_{Ic\ RT}$ MPa·m$^{0.5}$	$K_{Ic\ 1500}$ MPa·m$^{0.5}$	E GPa	$\alpha_{25-1300}$ 10^{-6}°C^{-1}	$K_{TH\ 25-1950}$ W/mK
ZB20	4.55	276±13	n.a.	4.25±0.07	n.a.	335±4	8.04 (‖) 10.58 (⊥)	n.a.
ZB50	3.42	129±3	219±23	4.32±0.27	6.09±0.17	129±4	6.35 (‖) 10.76 (⊥)	80–58 (‖) 41–46 (⊥)

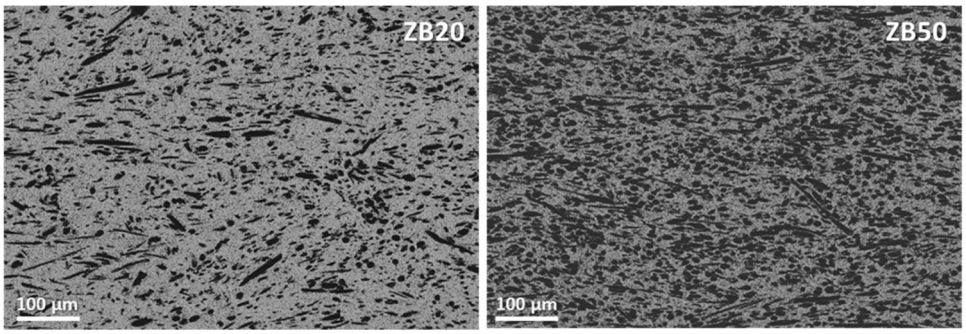

Fig. 3. SEM images of the cross sections of the ZrB_2-based CMCs containing 20 vol% (ZB20) and 50 vol% (ZB50) short carbon fiber.

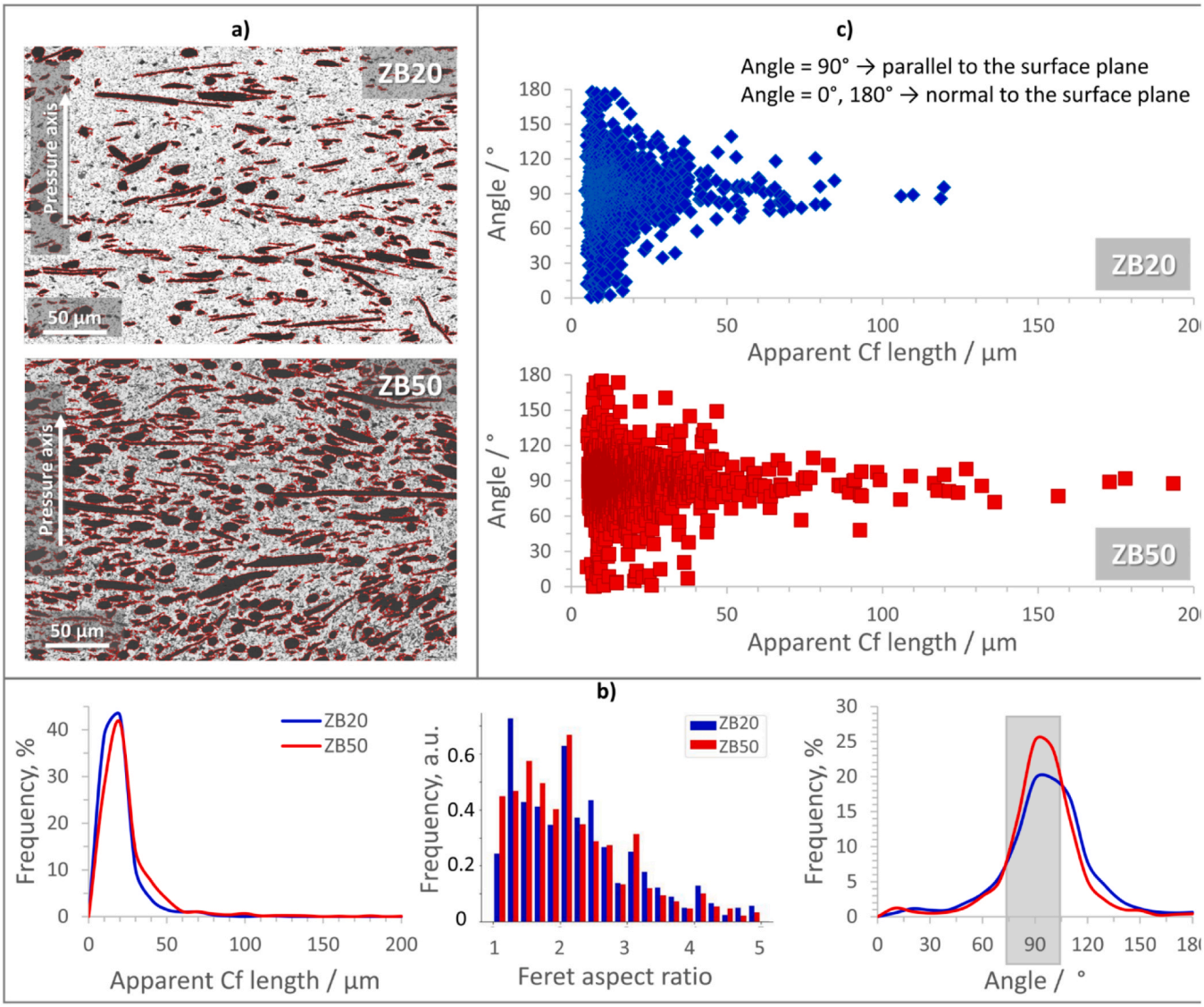

Fig. 4. a) SEM image of the cross plane sections of the ZB20 and ZB50 CMCs with segmented fibers as surrounded by ellipses fitted by the Analyze Particles module of the Image Pro Plus software; b) corresponding frequency distributions of fiber apparent length (or Feret's maximum length), Feret aspect ratio and angle orientation with the shaded area highlighting the different fractions of fiber oriented parallel to the surface in the two CMCs; c) the relation between misorientation angle and apparent fiber length.

content of ZB50 (higher number of interfaces), the C/μ values are higher than for ZB20 by a factor of 1.7. The ratio of the minimum to the maximum of the C/μ mean value for both specimen orientations is equal to 0.77. This implies that the degree of fiber orientation is independent of the fiber volume fractions. The fact that the minimum C/μ mean value is only a factor of 1/0.77 (~ 1.3) smaller than the maximum value indicates a certain degree of isotropy of the orientation. This fact can be either explained by some porosity in the specimens (porosity would

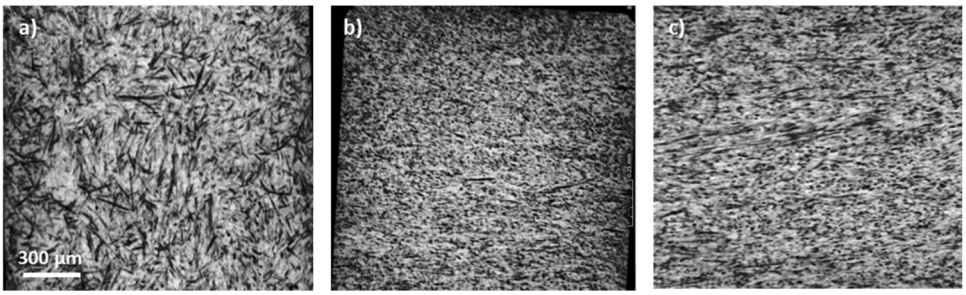

Fig. 5. a) Surface plane, and b) & c) cross planes of the reconstructed XCT data set of the specimen ZB20, with 20 vol% fiber volume. The fibers appear as dark areas.

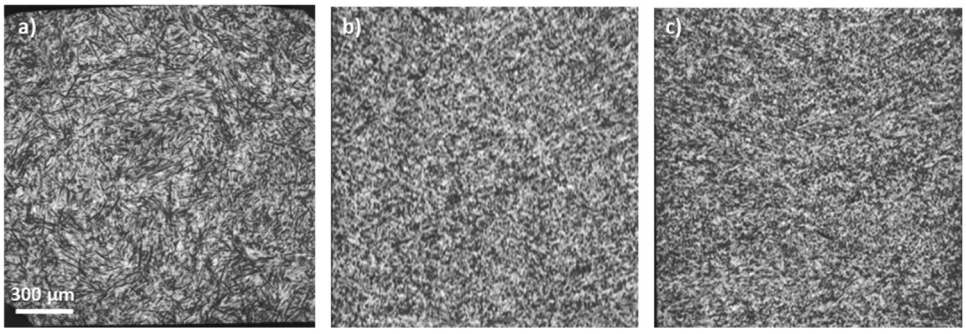

Fig. 6. a) Surface plane, and b) & c) cross planes of the reconstructed XCT data set of the specimen ZB50, with 50 vol% fiber volume. The fibers appear as dark areas.

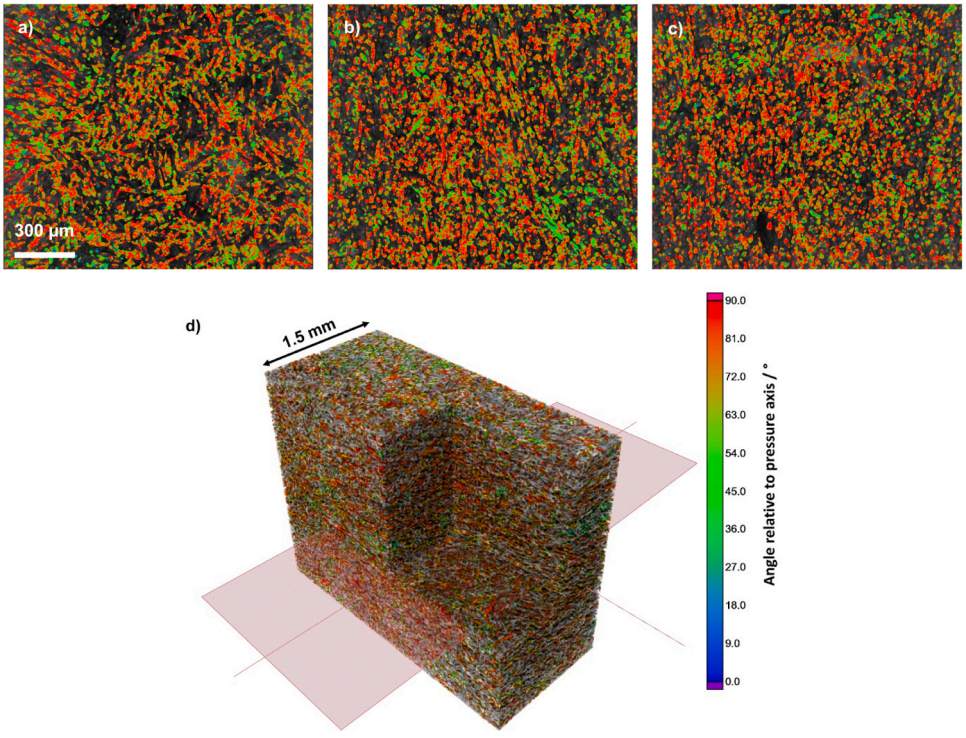

Fig. 7. Color-coded visualization of fiber orientation after segmentation a) in a surface plane, b) & c) in cross planes, and d) a 3D rendered representation within the ZB20 specimen. The color bar represents the angle between the local fiber orientation and the pressure axis. The red shaded plane represents the position of the surface plane displayed in a).

yield an isotropic X-ray refraction signal as a function of specimen orientation), or by the fact that several fibers lie perpendicular (or anyway strongly misaligned) to the main fiber orientation.

The results shown in Fig. 10 give a rough indication of the orientation of the fibers relative to the surface plane, as they only consider two perpendicular orientations.

As described in Section 2.2, the specimens were rotated around the X-ray beam for a more accurate fiber orientation analysis. The results are shown in Fig. 11 and Fig. 12: the mean intensity of the apparent transmission is represented as a function of the angle between the mean fiber

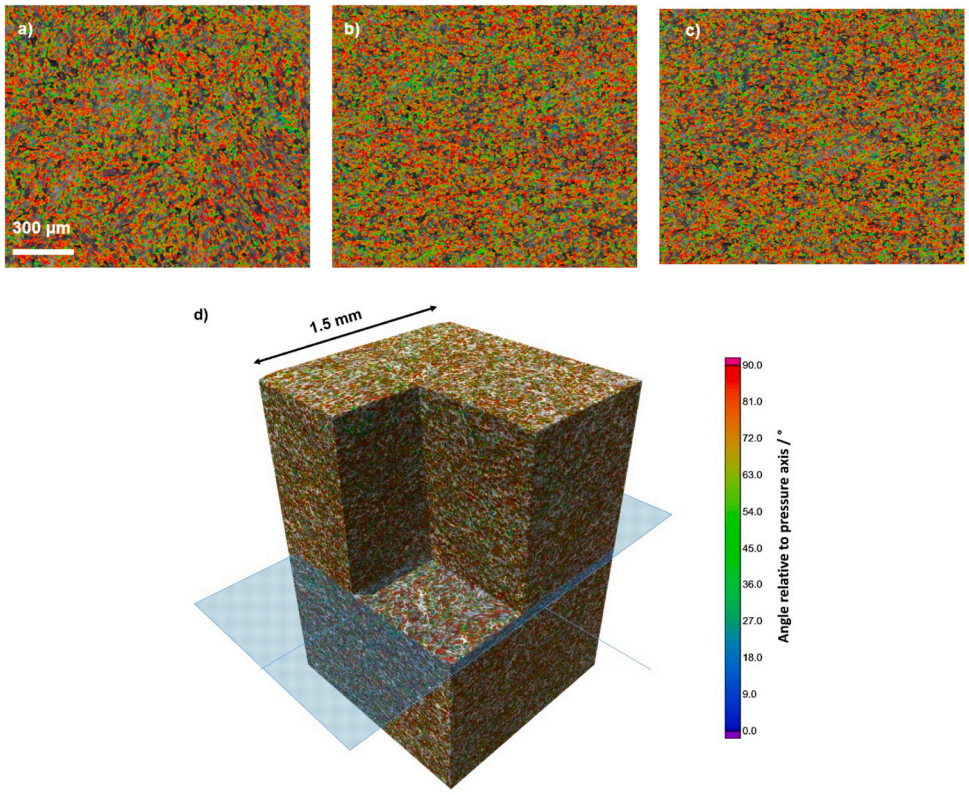

Fig. 8. Color-coded visualization of fiber orientation after segmentation a) in a surface plane, b) & c) in cross planes, and d) a 3D rendered representation within the ZB50 specimen. The color bar represents the angle between the local fiber orientation and the pressure axis. The blue shaded plane represents the position of the surface plane displayed in a).

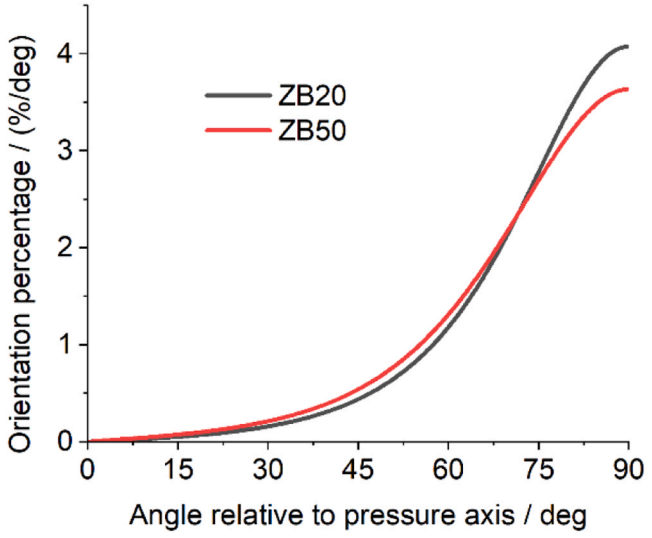

Fig. 9. Comparison of the fiber alignment of specimens ZB20 and ZB50: histograms of the local fiber orientation normalized to the total number of voxels assigned to fibers as function of the deviation angle from the pressure axis (see Fig. 7 and Fig. 8).

orientation and the scattering vector.

The signal of the apparent transmission is largest when the fibers are oriented perpendicular (90° and 270°) and smallest when the fibers are oriented parallel (0° and 180°) to the scattering vector **Q**. The width of the extrema of the curves indicates that the fiber orientation distribution is indeed not a Dirac's delta, but a considerable fraction of fibers is oriented with their main axis outside the surface plane.

Table 3
Statistics of fiber orientation in the specimens ZB20 and ZB50: the 50th, 75th, and 90th percentiles of the fiber orientation are given relative to the pressure axis and mean orientation tensors, where the third component points along the pressure axis. MOT: mean orientation tensor.

	ZB 20	ZB50	ZB 20	ZB50
	percentile /deg		M	
50th	75.0	76.6	$\begin{pmatrix} 0.43 & -0.02 & -0.02 \\ -0.02 & 0.45 & 0.04 \\ -0.02 & 0.04 & 0.13 \end{pmatrix}$	$\begin{pmatrix} 0.42 & 0 & 0.01 \\ 0 & 0.43 & 0.02 \\ 0.01 & 0.02 & 0.14 \end{pmatrix}$
75th	83.1	83.9		
90th	87.4	87.7		

3.4. Comparison among the techniques

In general, SEM images, XCT reconstructions, and SXRR provide consistent information concerning the fiber orientation, although they capture the properties of the specimens in different ways: SEM images capture a specific 2D section; XCT provides 3D volume in the bulk of the specimens; X-ray refraction radiographs show a signal integrated over the specimen thickness, thereby providing information in 2.5D, that is with high lateral resolution (in 2 dimensions perpendicular to the beam) and integrated along the third dimension (beam direction).

On one hand, SEM images show a small field-of-view, but with extraordinary high resolution and with a high degree of detail, whereas SXRR images are indirect but encompass a much larger and statistically significant field-of-view.

The evaluation of the SEM images is very time-consuming, around 3 hours for having the final information, and might not always be representative of the full volume, for example in case of fiber agglomeration. On the other hand, XCT and SXXR require about 3 hours and 1.5 hours, respectively to obtain the requested results, but considering a much larger volume of material (for the same volume/area one would require a much larger time for the analysis of SEM images).

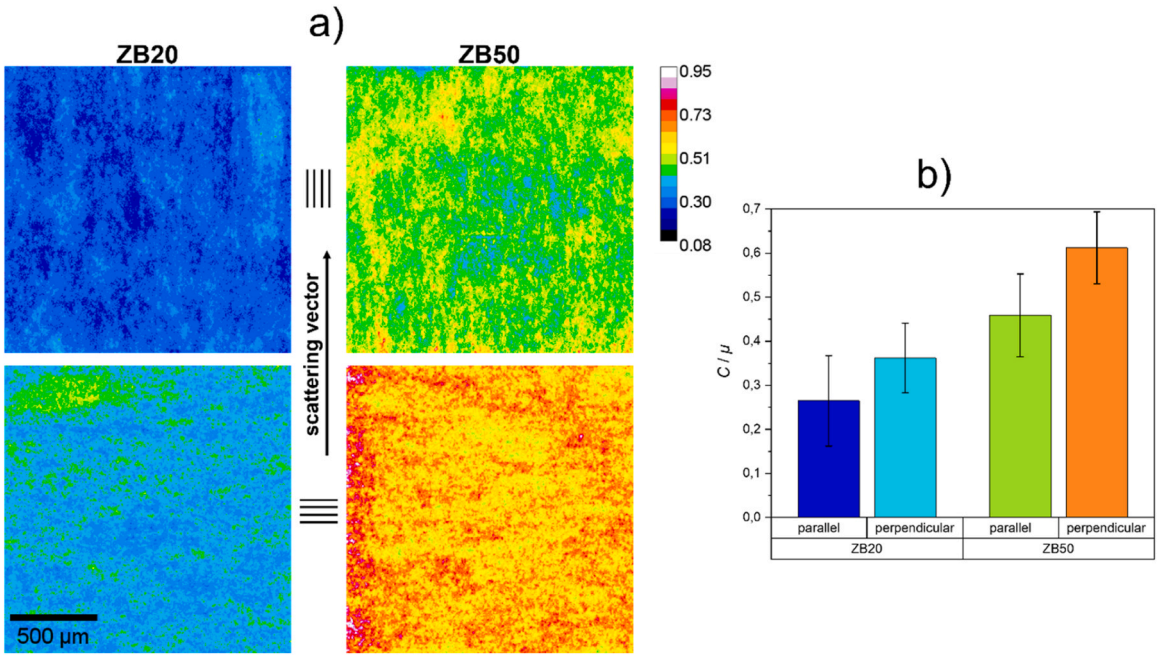

Fig. 10. a) Color-coded 2D distribution of C/µ for fibers parallel (top) and perpendicular (bottom) to the scattering vector. The color scale is identical for both orientations. b) Mean values of C/µ over the whole images in a) are given as bar graphs. The error bars in the graphs represent the inhomogeneity of the C/µ values over the fields-of-view.

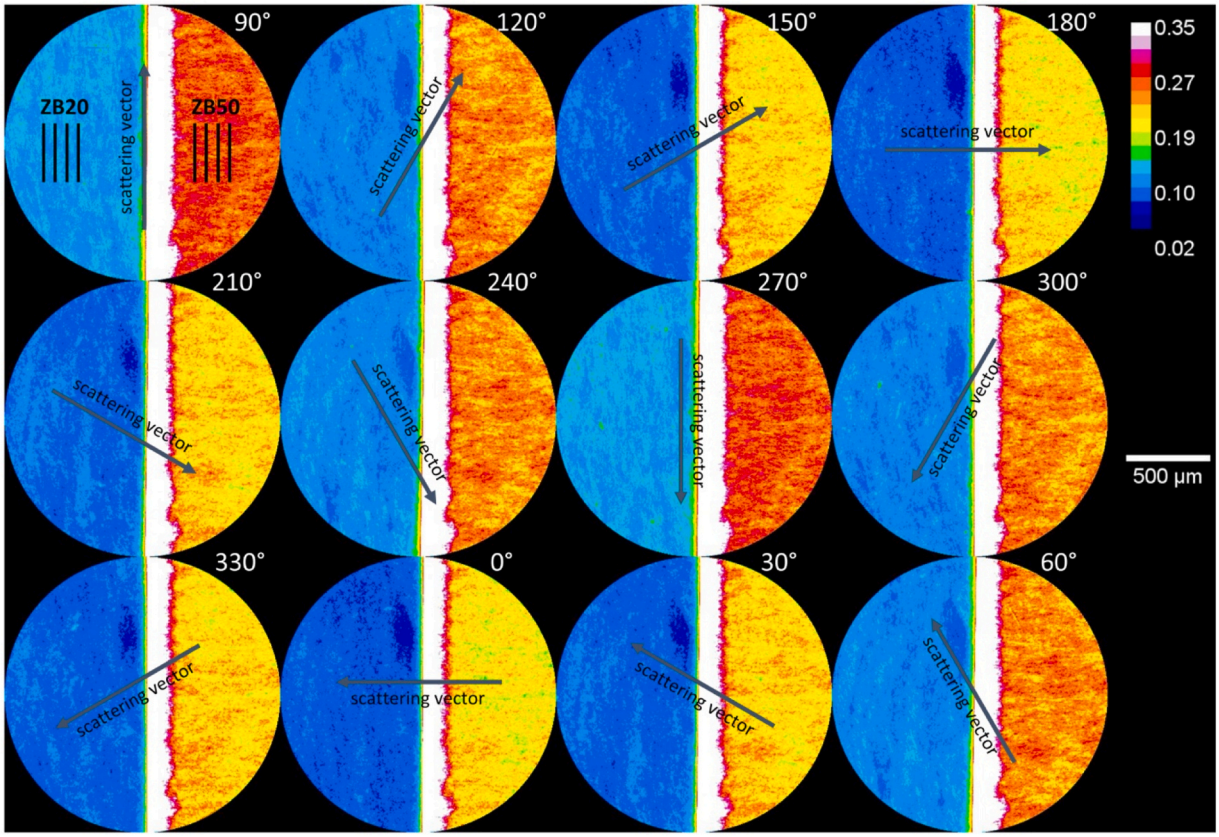

Fig. 11. 2D distribution of the apparent transmission signal (see text) as a function of the orientation of the scattering vector. The left side of each disc represents the ZB20, the right side the ZB50 specimen. The nominal fiber orientation inside the specimen is indicated by the 4 lines in the image labeled 90°.

SXRR reaches its limit when one wants to examine heavier matrix materials, such as Hf- and Ta- based borides and carbides. In our study, the thickness of the ZrB_2-based specimens was about 200 µm; for heavier matrix materials, thinner platelets would be necessary, thereby undermining the statistical significance of the results. However, SXRR was developed to be used on lightweight materials, in particular CMCs, with

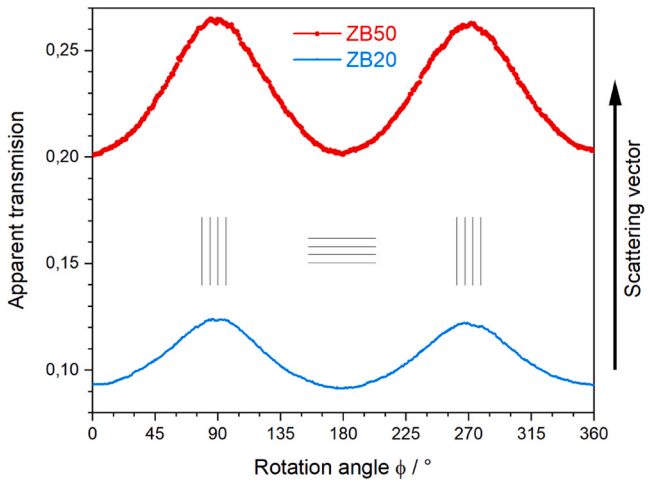

Fig. 12. Apparent transmission mean value of the images in Fig. 11 (acquired at orientation intervals of 1°); the nominal fiber orientation with respect to the scattering vector is indicated by the 4 parallel lines.

very low X-ray attenuation and poor contrast among constituents. In recent times even steel and Ni, with density in the 7.5–8.9 g/cm^3 range, could be imaged using specimens of thicknesses above 200 μm. It should be mentioned that the fiber orientation distributions (FOD) derived from microscopy, XCT, and SXRR cannot be directly compared since SEM and SXRR data is obtained from single 2D sections and projections, respectively. Table 4 lists some characteristics of the FODs obtained from the three imaging techniques used in this study.

The fiber orientation and spatial distributions obtained from XCT and SXRR images can be used as input for finite element method (FEM) analysis of mechanical and thermal properties. This cannot be achieved with conventional SEM outputs. The concurrent use of 3D and 2.5D information can also provide separate information on the kind of features (pores, cracks or fiber interfaces) present in the microstructure of the material, so that a combination of all techniques is recommended for a thorough characterization.

4. Conclusions

In this work, we determined the orientation distribution of short carbon fibers in ZrB_2 matrix materials with two different fiber concentrations, 20 and 50 vol%. Three imaging techniques were used: Scanning Electron Microscopy (SEM), X-ray Computed Tomography (XCT), and Synchrotron X-ray Refraction Radiography (SXRR). We found that, while the short fibers were aligned in a plane perpendicular to the pressure applied during processing, their distribution in the CMCs spanned over a large interval. Such interval was similar for the two materials investigated, despite the low and high fiber volume fractions.

We observed that fibers lay within the surface plane (perpendicular to the pressure axis) more easily if the fiber volume fraction is lower; we quantified the deviations to be about ±20° for the composite with 20% fiber volume fraction and ±25° for the one with 50% fiber fraction. Thanks to the 3D analysis carried out by X-ray computed tomography, we could also infer a correlation between fiber shape (aspect ratio) and orientation distribution. We could obtain mean fiber orientation tensors for both materials investigated and quantified the degree of cylindrical symmetry of the fiber distributions. Through the use of synchrotron radiation refraction radiography, we could obtain one-dimensional pole figures of the fiber orientations, as well as an estimation of the inhomogeneity of such distribution within the specimens.

We finally compared the three imaging techniques and discussed their advantages and limitations in this specific case. SEM enables imaging fibers separately, XCT provides 3D information of the fiber distribution in the bulk, and SXRR enables imaging a large field of view, inaccessible to the other two techniques. It is concluded that the three techniques well complement each other and are recommended for a thorough microstructural characterization of CMCs.

We stress that SXRR and XCT data can well be input in FEM codes and physical-model-based simulation programs, as they yield statistically relevant information.

Table 4
Comparison of the fiber orientation distributions (FOD) according to different investigation methods.

	FOD	Orientation	Statistical significance
Microscopy	quantitative	in surface planes	low
XCT	qualitative	relative to pressure axis	high
SXRR	quantitative	relative to pressure axis	high

CRediT authorship contribution statement

Laura Silvestroni: Conceptualization, Formal Analysis, Investigation, Data curation, Writing – original draft, Writing – review & editing, Visualization, Funding acquisition. **Andreas Kupsch:** Conceptualization, Formal Analysis, Investigation, Data curation, Writing – original draft, Writing – review & editing, Visualization. **Bernd R. Müller:** Formal Analysis, Investigation, Data curation, Writing – original draft, Writing – review & editing, Visualization. **Alexander Ulbricht:** Investigation, Data curation, Writing – review & editing. **Frank Wieder:** Formal Analysis, Data curation, Visualization. **Tobias Fritsch:** Formal Analysis, Investigation, Data curation, Writing – review & editing, Visualization. **Diletta Sciti:** Writing – review & editing. **Giovanni Bruno:** Conceptualization, Writing – original draft, Writing – review & editing.

Declaration of Competing Interest

The authors declare that they have no known competing financial interests or personal relationships that could have appeared to influence the work reported in this paper.

Acknowledgments

Research was jointly sponsored by the U.S. Army DEVCOM and by the U.S. ONR and was accomplished under the Cooperative Agreement n. W911NF-19–2–0253 with Amanda Napier and Eric Wuchina as contract monitors. The views and conclusions contained in this document are those of the authors and should not be interpreted as representing the official policies, either expressed or implied, of the U.S. Army DEVCOM, U.S. ONR or the U.S Government. The U.S. Government is authorized to reproduce and distribute reprints for Government purposes notwithstanding any copyright notation herein. Michael Sintschuk and Ralf Britzke (BAM) are acknowledged for their assistance during beam time at BAMline. Open Access funding enabled and organized by Projekt DEAL.

References

[1] B.R. Golla, A. Mukhopadhyay, B. Basu, S.K. Thimmappa, Review on ultra-high temperature boride ceramics, Prog. Mater. Sci. 111 (2020) 100651.
[2] E. Wuchina, E. Opila, M. Opeka, W. Fahrenholtz, I. Talmy, UHTCs: ultra-high temperature ceramic materials for extreme environment applications, Electrochem. Soc. Interface 16 (4) (2007) 30–36.
[3] S.R. Levine, E.J. Opila, M.C. Halbig, J.D. Kiser, M. Singh, J.A. Salem, Evaluation of ultra-high temperature ceramics for aeropropulsion use, J. Eur. Ceram. Soc. 22 (14-15) (2002) 2757–2767.
[4] J.J. Sha, J. Li, S.H. Wang, Z.F. Zhang, Y.F. Zu, S. Flauder, W. Krenkel, Improved microstructure and fracture properties of short carbon fiber-toughened ZrB2-based UHTC composites via colloidal process, Int. J. Refract. Met. Hard Mater. 60 (2016) 68–74.
[5] J.J. Sha, J. Li, Z.Z. Lv, S.H. Wang, Z.F. Zhang, Y.F. Zu, S. Flauder, W. Krenkel, ZrB2-based composites toughened by as-received and heat-treated short carbon fibers, J. Eur. Ceram. Soc. 37 (2) (2017) 549–558.

[6] D.W. Ni, Y. Cheng, J.P. Zhang, J.X. Liu, J. Zou, B.W. Chen, H.Y. Wu, H.J. Li, S. M. Dong, J.C. Han, X.H. Zhang, Q.G. Fu, G.J. Zhang, Advances in ultra-high temperature ceramics, composites, and coatings, J. Adv. Ceram. 11 (1) (2022) 1–56.
[7] S. Mungiguerra, L. Silvestroni, R. Savino, L. Zoli, B. Esser, M. Lagos, D. Sciti, Qualification and reusability of long and short fibre-reinforced ultra-refractory composites for aerospace thermal protection systems, Corros. Sci. 195 (2022) 16.
[8] L.M. Rueschhoff, C.M. Carney, Z.D. Apostolov, M.K. Cinibulk, Processing of fiber-reinforced ultra-high temperature ceramic composites: a review, Int. J. Ceram. Eng. Sci. 2 (2020) 22–37.
[9] Y. Shi, K. Tushtev, D. Koch, Characterization of mechanical properties under shear load of a short-carbon-fiber-reinforced C/SiC ceramic, J. Ceram. Sci. Technol. 6 (3) (2015) 183–189.
[10] Y. Shi, J.M. Hausherr, H. Hoffmann, D. Koch, Inspection of geometry influence and fiber orientation to characteristic value for short fiber reinforced ceramic matrix composite under bending load, J. Eur. Ceram. Soc. 37 (4) (2017) 1291–1303.
[11] S. Flauder, N. Langhof, W. Krenkel, S. Schafföner, Size effect of carbon fiber-reinforced silicon carbide composites (C/C-SiC): part 1-bending load and statistical effects, J. Eur. Ceram. Soc. 41 (14) (2021) 6805–6814.
[12] S. Flauder, I. Bombarda, R. D'Ambrosio, N. Langhof, A. Lazzeri, W. Krenkel, S. Schafföner, Size effect of carbon fiber-reinforced silicon carbide composites (C/C-SiC): part 2-tensile testing with alignment device, J. Eur. Ceram. Soc. 42 (4) (2022) 1227–1237.
[13] S. Flauder, F. Wich, J.J. Sha, N. Langhof, W. Krenkel, S. Schafföner, Effect of thermo-mechanical and low-cycle preloading on the strength of carbon fiber-reinforced ceramic matrix composites, J. Eur. Ceram. Soc. 43 (13) (2023) 5474–5483.
[14] W.Q. Pan, X.Z. Xia, W. Zhou, Y. Li, Effect of fiber orientation on tribological properties of fiber-reinforced C/C-SiC composites mated with ceramic ball, J. Am. Ceram. Soc. 107 (1) (2024) 593–603.
[15] S.-Y. Fu, X. Hu, C.-Y. Yue, Effects of fiber length and orientation distributions on the mechanical properties of short-fiber reinforced polymers- a review, Mater. Sci. Res. Int. 5 (2) (1999) 74–83.
[16] S.Y. Fu, B. Lauke, Effects of fiber length and fiber orientation distributions on the tensile strength of short-fiber-reinforced polymers, Compos. Sci. Technol. 56 (10) (1996) 1179–1190.
[17] W. Zhou, M. Meiser, F. Wich, T. Liensdorf, W. Freudenberg, Y. Li, N. Langhof, W. Krenkel, Fiber orientation dependence of tribological behavior of short carbon fiber reinforced ceramic matrix composites, J. Am. Ceram. Soc. 105 (1) (2022) 538–552.
[18] J. Winkelbauer, G. Puchas, S. Schafföner, W. Krenkel, Short fiber-reinforced oxide fiber composites, Int. J. Appl. Ceram. Technol. 19 (2) (2022) 1136–1147.
[19] M.A. Lagos, C. Pellegrini, I. Agote, N. Azurmendi, J. Barcena, M. Parco, L. Silvestroni, L. Zoli, D. Sciti, Ti_3SiC_2-Cf composites by spark plasma sintering: processing, microstructure and thermo-mechanical properties, J. Eur. Ceram. Soc. 39 (9) (2019) 2824–2830.
[20] L. Silvestroni, A. Vinci, S. Failla, L. Zoli, V. Rubio, J. Binner, D. Sciti, Ablation behaviour of ultra-high temperature ceramic matrix composites: role of $MeSi_2$ addition, J. Eur. Ceram. Soc. 39 (9) (2019) 2771–2781.
[21] F. De Bianchi, S.A. Ponnusami, L. Silvestroni, A.M. Grande, Thermo-elastic properties in short fibre reinforced ultra-high temperature ceramic matrix composites: characterisation and numerical assessment, Mater. Today Commun. 29 (2021) 9.
[22] L. Silvestroni, D. Pavan, C. Melandri, D. Sciti, N. Gilli, L. Ortiz-Membrado, E. Jimenez-Pique, A.M. Grande, Functionally graded ultra-high temperature ceramics: from thermo-elastic numerical analysis to damage tolerant composites, Mater. Des. 224 (2022) 13.
[23] B.N. Sharma, D. Naragani, B.N. Nguyen, C.L. Tucker, M.D. Sangid, Uncertainty quantification of fiber orientation distribution measurements for long-fiber-reinforced thermoplastic composites, J. Compos Mater. 52 (13) (2018) 1781–1797.
[24] T. Mishurova, N. Rachmatulin, P. Fontana, T. Oesch, G. Bruno, E. Radi, I. Sevostianov, Evaluation of the probability density of inhomogeneous fiber orientations by computed tomography and its application to the calculation of the effective properties of a fiber-reinforced composite, Int. J. Eng. Sci. 122 (2018) 14–29.
[25] H. Bale, M. Blacklock, M.R. Begley, D.B. Marshall, B.N. Cox, R.O. Ritchie, Characterizing three-dimensional textile ceramic composites using synchrotron X-ray micro-computed-tomography, J. Am. Ceram. Soc. 95 (1) (2012) 392–402.
[26] F. Léonard, J. Stein, C. Soutis, P.J. Withers, The quantification of impact damage distribution in composite laminates by analysis of X-ray computed tomograms, Compos. Sci. Technol. 152 (2017) 139–148.
[27] D. Ekenhorst, J. Goebbels, H. Riesemeier, B. Illerhaus, Computerized cone beam tomography of ceramic matrıx composites, Mater. Test. 37 (4) (1995) 118–122.
[28] M. Krause, J.M. Hausherr, B. Burgeth, C. Herrmann, W. Krenkel, Determination of the fibre orientation in composites using the structure tensor and local X-ray transform, J. Mater. Sci. 45 (4) (2010) 888–896.
[29] J.M. Hausherr, W. Krenkel, F. Fischer, V. Altstadt, Nondestructive characterization of high-performance C/SiC-ceramics using X-ray-computed tomography, Int. J. Appl. Ceram. Technol. 7 (3) (2010) 361–368.
[30] F. Wan, T.J. Pirzada, R.J. Liu, Y.F. Wang, C.R. Zhang, T.J. Marrow, Microstructure Characterization by X-ray computed tomography of C/C-SiC ceramic composites fabricated with different carbon fiber architectures, Appl. Compos. Mater. 26 (4) (2019) 1247–1260.
[31] Y. Chen, Y. Shi, C. Chateau, J. Marrow, In situ X-ray tomography characterisation of 3D deformation of C/C-SiC composites loaded under tension, Compos. Pt. A-Appl. Sci. Manuf. 145 (2021) 13.
[32] V. Sodisetty, A.K. Singh, H. James, K.L. Lee, Z. Benedict, Damage evolution in quasi-statically indented alumina based oxide/oxide ceramic matrix composites: an experimental investigation, Ceram. Int. 48 (21) (2022) 32491–32503.
[33] B.R. Müller, R.C. Cooper, A. Lange, A. Kupsch, M. Wheeler, M.P. Hentschel, A. Staude, A. Pandey, A. Shyam, G. Bruno, Stress-induced microcrack density evolution in β-eucryptite ceramics: experimental observations and possible route to strain hardening, Acta Mater. 144 (Supplement C) (2018) 627–641.
[34] A. Kupsch, B.R. Müller, A. Lange, G. Bruno, Microstructure characterisation of ceramics via 2D and 3D X-ray refraction techniques, J. Eur. Ceram. Soc. 37 (5) (2017) 1879–1889.
[35] A.P. Soares, D. Baum, B. Hesse, A. Kupsch, B.R. Müller, P. Zaslansky, Scattering and phase-contrast X-ray methods reveal damage to glass fibers in endodontic posts following dental bur trimming, Dent. Mater. 37 (2) (2021) 201–211.
[36] A. Kupsch, A. Lange, M.P. Hentschel, Y. Onel, T. Wolk, A. Staude, K. Ehrig, B. R. Müller, G. Bruno, Evaluating porosity in cordierite diesel particulate filter materials, part 1 X-ray refraction, J. Ceram. Sci. Technol. 4 (4) (2013) 169–176.
[37] S. Evsevleev, B.R. Müller, A. Lange, A. Kupsch, Refraction driven X-ray caustics at curved interfaces, Nucl. Instrum. Methods Phys. Res. Sect. A: Accel., Spectrom., Detect. Assoc. Equip. 916 (2019) 275–282.
[38] R. Laquai, B.R. Müller, J.A. Schneider, A. Kupsch, G. Bruno, Using SXRR to probe the nature of discontinuities in SLM additive manufactured inconel 718 specimens, Metall. Mater. Trans. A 51 (8) (2020) 4146–4157.
[39] A. Kupsch, V. Trappe, B.R. Müller, G. Bruno, Evolution of CFRP stress cracks observed by in-situ X-ray refractive imaging, IOP Conference Series: Materials Science and Engineering 942 (2020) 012035 https://iopscience.iop.org/article/10.1088/1757-899X/942/1/012035/meta.
[40] J. Nellesen, R. Laquai, B.R. Müller, A. Kupsch, M.P. Hentschel, N.B. Anar, E. Soppa, W. Tillmann, G. Bruno, In situ analysis of damage evolution in an Al/Al2O3 MMC under tensile load by synchrotron X-ray refraction imaging, J. Mater. Sci. 53 (8) (2018), 6021-2461.
[41] I. Serrano-Munoz, I. Roveda, A. Kupsch, B.R. Müller, G. Bruno, Synchrotron X-ray refraction detects microstructure and porosity evolution during in-situ heat treatments, Mater. Sci. Eng.: A 838 (2022) 142732.
[42] R. Laquai, T. Schaupp, A. Griesche, B.R. Müller, A. Kupsch, A. Hannemann, T. Kannengiesser, G. Bruno, Quantitative analysis of hydrogen-assisted microcracking in duplex stainless steel through X-ray refraction 3D imaging, Adv. Eng. Mater. 24 (6) (2022) 2101287.
[43] V. Voland, M. Salamon, S. Reisinger, S. Schröpfer, N. Uhlmann, Novel Techniques for High-resolution computed tomography of optoelectronic devices, In: Proceedings of the 18th World Conference on Nondestructive Testing, Durban, South Africa, 2012.
[44] L.A. Feldkamp, L.C. Davis, J.W. Kress, Practical cone-beam algorithm, J. Opt. Soc. Am. A 1 (6) (1984) 612–619.
[45] W. Görner, M.P. Hentschel, B.R. Müller, H. Riesemeier, M. Krumrey, G. Ulm, W. Diete, U. Klein, R. Frahm, BAMline: the first hard X-ray beamline at BESSY II, Nucl. Instrum. Methods Phys. Res. Sect. A-Accel. Spectrom. Dect. Assoc. Equip. 467 (2001) 703–706.
[46] H. Markötter, B.R. Müller, A. Kupsch, S. Evsevleev, T. Arlt, A. Ulbricht, S. Dayani, G. Bruno, A review of X-ray imaging at the BAMline (BESSY II), Adv. Eng. Mater. 22 (2023).
[47] D. Chapman, W. Thomlinson, R.E. Johnston, D. Washburn, E. Pisano, N. Gmur, Z. Zhong, R. Menk, F. Arfelli, D. Sayers, Diffraction enhanced x-ray imaging, Phys. Med. Biol. 42 (11) (1997) 2015–2025.
[48] L. Rigon, H.J. Besch, F. Arfelli, R.H. Menk, G. Heitner, H. Plothow-Besch, A new DEI algorithm capable of investigating sub-pixel structures, J. Phys. D. -Appl. Phys. 36 (10A) (2003) A107–A112.
[49] L. Rigon, F. Arfelli, R.H. Menk, Generalized diffraction enhanced imaging to retrieve absorption, refraction and scattering effects, J. Phys. D. -Appl. Phys. 40 (10) (2007) 3077–3089.
[50] A. Zocca, B.R. Müller, R. Laquai, A. Kupsch, F. Wieder, S. Benemann, J. Wilbig, J. Gunster, G. Bruno, Microstructural characterization of AP40 apatite-wollastonite glass-ceramic, Ceram. Int. 49 (8) (2023) 12672–12679.
[51] A. Lange, M.P. Hentschel, A. Kupsch, B.R. Müller, Numerical correction of X-ray detector backlighting, Int. J. Mater. Res. 103 (2) (2012) 174–178.
[52] A.M. Al-Falahat, A. Kupsch, M.P. Hentschel, A. Lange, N. Kardjilov, H. Markötter, I. Manke, Correction approach of detector backlighting in radiography, Rev. Sci. Instrum. 90 (12) (2019) 125108.
[53] D. Mani, A. Kupsch, B.R. Müller, G. Bruno, Diffraction enhanced imaging analysis with pseudo-Voigt fit function, J. Imaging 8 (8) (2022) 206.
[54] F. Arfelli, L. Rigon, R.H. Menk, Microbubbles as x-ray scattering contrast agents using analyzer-based imaging, Phys. Med. Biol. 55 (6) (2010) 1643–1658.
[55] F. Arfelli, A. Astolfo, L. Rigon, R.H. Menk, A. Gaussian, Extension for diffraction enhanced imaging, Sci. Rep. 8 (2018) 14.
[56] H. Chen, B. Liu, L.M. Zhao, K. Ren, Z.L. Wang, Retrieval of multiple scattering contrast from x-ray analyzer-based imaging, Chin. Phys. B 30 (1) (2021) 018701.
[57] L.M. Zhao, T.X. Wang, R.K. Ma, Y. Gu, M.S. Luo, H. Chen, Z.L. Wang, X. Ge, Analysis of refraction and scattering image artefacts in x-ray analyzer-based imaging, Chin. Phys. B 32 (2) (2023) 028701.
[58] L. Silvestroni, D.D. Fabbriche, C. Melandri, D. Sciti, Relationships between carbon fiber type and interfacial domain in ZrB_2-based ceramics, J. Eur. Ceram. Soc. 36 (1) (2016) 17–24.